Electronic and magnetotransport properties of twisted bilayer graphene in the presence of external electric and magnetic fields

Priyanka Sinha [1,*] Ayan Mondal [1,†] Simão Meneses João,[2] and Bheema Lingam Chittari[1,‡]
[1]*Department of Physical Sciences, Indian Institute of Science Education and Research Kolkata, Mohanpur-741246, West Bengal, India*
[2]*Department of Materials, Imperial College London, South Kensington Campus, London SW7 2AZ, United Kingdom*

(Received 16 November 2023; revised 15 March 2024; accepted 21 March 2024; published 10 April 2024)

We investigate extensively the electronic and transport properties of twisted bilayer graphene when subjected to both an external perpendicular electric field and a magnetic field. Using a basic tight-binding model, we show the flat electronic band properties as well as the density of states (DOS), both without and with the applied electric field. In the presence of an electric field, the degeneracy at the Dirac points is lifted and a nonmonotonic behavior is found in the energy shift between the Dirac points of each layer, especially for twist angles below 3°. We also study the behavior of the Landau levels (LL) spectra for different twist angles within a very low energy range. These LL spectra get modified under the influence of the external electric field. Moreover, we calculate the dc Hall conductivity (σ_{xy}) for a very large system using the kernel polynomial method. Interestingly, as we tune the twist angle from a higher to a lower value, σ_{xy} undergoes a transition from a half-integer to an integer quantum Hall effect, i.e., the value of σ_{xy} shifts from $\pm 4(n + 1/2)$ $(2e^2/h)$ (n is an integer) to $\pm 2n$ $(2e^2/h)$ around a small twist angle of $\theta = 2.005°$. At this angle, σ_{xy} acquires a Hall plateau at zero Fermi energy. However, the behavior of σ_{xy} remains unaltered when the system is exposed to the electric field, particularly at the magic angle where the bands in both layers can hybridize, and strong interlayer coupling plays a crucial role.

DOI: 10.1103/PhysRevB.109.155412

I. INTRODUCTION

Since the discovery of graphene [1–3], van der Waals (vdW) layered materials [4] have been at the forefront of scientific interest. Among these, twisted bilayer graphene (TBG) [5–8] is one such heterostructure that stands out due to its remarkable band properties. These properties encompass the coexisting massive and massless Dirac fermions [9], second-generation Dirac singularities [10], the Hofstadter butterfly spectrum [11], the coexistence of superlattice Dirac points and Van Hove singularities (VHS) [12], etc. In TBG, two graphene layers are rotated at a specific angle relative to each other, resulting in the formation of a moiré pattern. This pattern can be visualized using scanning tunneling microscopy [13,14], and it exhibits a periodic nature, with larger periods observed at smaller twist angles [15]. Moreover, the twist angle impacts the position of the Dirac cones in each layer, causing a displacement in momentum [16]. Several methods, including growth on the C face of a SiC substrate [17,18], chemical vapor deposition (CVD) growth techniques on metal substrates [19–22], or mechanical folding of a monolayer graphene sheet [23], etc., have been used to produce TBG structures. In TBG, collective charge carrier behavior arises from the flat regions of the band structure near a saddle point, where multiple electrons share the same energy level being highly localized at the AA sites [24]. Experimentally, the localization of electrons and the VHS in twisted graphene layers have been measured by scanning tunneling spectroscopy [13,25]. The nearly flat low-energy bands in the moiré pattern formed by twisted graphene layers, referred to as magic-angle twisted bilayer graphene (MATBG) [6], give rise to a physics of strong correlation [26,27]. There is evidence of Mott-like insulating behavior [28], superconductivity [29], the anomalous Hall effect [30], etc., which corroborates the richness of the physics it possesses.

The low-energy electronic structure of TBG possesses massless Dirac fermions, albeit with a diminished Fermi velocity compared to monolayer graphene at small twist angles [5,24,31], which is quite different from that of an AB-stacked bilayer graphene. Both theoretical and experimental studies have demonstrated the alteration of the band gap in bilayer graphene due to the different on-site energies between the layers [32,33]. There are records of the possibility of controlling the band gap of Bernal bilayer graphene by applying the electric field [34–36]. However, contrary to this, an external electric field does not induce a band gap in the band structure of TBG [37]. Nevertheless, the presence of an interlayer bias gives rise to exotic phenomena, such as additional anisotropic reduction of the Fermi velocity [38], the emergence of topologically protected helical modes [39], 12-fold symmetry breaking of quasicrystalline states [40], etc., in the electronic spectrum. Recent findings also suggest that large-angle TBG may offer semiconductor-like behavior with tunable band gaps up to terahertz frequencies when subjected to an electric field [41]. The combination of gate tunability [42–44] and twist angle in certain two-dimensional systems has demonstrated the possibility of achieving

*sinhapriyanka2012@gmail.com
†ayanmondal367@gmail.com
‡bheemalingam@iiserkol.ac.in

tunable Mott insulators [42], as well as topological flat bands [45], etc.

On the other side, the discovery of an unusual quantum Hall effect in monolayer graphene provides evidence for the existence of massless Dirac fermions [46], whereas, in the case of bilayer graphene, the quantization rules for the integer quantum Hall effect are quite different, confirming the characteristics of massive quasiparticles [47]. The Landau level (LL) energies vary as $E_n \sim \pm\sqrt{|n|B}$ (B is the strength of the magnetic field, n is the LL index) and $E_n \sim \pm\hbar\omega\sqrt{n(n-1)}$ ($\omega = eB/m$ is the cyclotron frequency) for the monolayer and bilayer graphene, respectively. However, the role of interlayer coupling becomes crucial in the formation of LL spectra as it influences the behavior of quasiparticles of a pristine TBG [5,48]. Strikingly, the massless Dirac fermions still survive in TBG for large twist angles due to the decoupling of twisted layers [49]. When exposed to a perpendicular magnetic field, the electronic behavior of TBG remains similar to that of a monolayer for twist angles exceeding 20° [25]. Experimentally, the behavior of the LLs has been addressed using scanning tunneling microscopy and LL scanning tunneling spectroscopy depending on the twist angle [25]. Several studies have been reported on the LL spectrum as well as the Hall quantization of TBG, both through analytical and experimental approaches [48,50–54]. Furthermore, the dc conductivity has been studied for different twist angles in the presence of disorder [55–57]. Previous works [58,59] have addressed magnetotransport in small-angle TBG when the applied bias causes topological channels to appear [60]. However, a more comprehensive study of the combined effect of electric field and magnetic field in the magic-angle TBG has yet to be explored.

In this paper, we investigate the effects of a perpendicular electric field and a magnetic field on the electronic and transport characteristics of TBG in the mesoscopic regime, using a real-space large-scale approach to quantum transport. We predict the first magic angle and study the electronic band structure and the density of states (DOS) characteristics pertaining to the magic angle, as well as for adjacent small twist angles (both below and above the magic angle). Next, we introduce a perpendicular electric field into the system to investigate its influence on the electronic properties. Notably, we observe nonmonotonic dispersion of energy levels with varying electric field strength. In the presence of a weak magnetic field, we show the DOS spectrum for the magic angle and also investigate the LL spectra for different twist angles. We also unveil novel effects of the electric field on the LL spectrum for the magic angle. Subsequently, we employ the real-space method to calculate the dc Hall conductivity within the linear-response regime, utilizing the Kubo-Bastin formula [61,62], as implemented in KITE [63–65]. Nevertheless, we reveal the transport behavior in the TBG system with a significant number of unit cells. This underscores the complexities that emerge from modeling such structures, especially near the magic angle, which creates a high demand for research.

The paper is organized as follows. The geometry and the model Hamiltonian of TBG are introduced in Sec. II. In Sec. III, we describe the formalism to compute the transport properties and the DOS in detail. Our results are presented in Sec. IV. Sections IV A and IV B include the results for the band structures and the DOS in the absence ($U = 0$) and presence ($U \neq 0$) of an external electric field, respectively. The effects of a perpendicular magnetic field ($B \neq 0$) are depicted through the LL spectra shown in Sec. IV C. To illustrate the effects of both electric and magnetic fields simultaneously on the LL spectra, we observed the density of states in Sec. IV D. Further, the transport properties are investigated by computing the dc Hall conductivities in Sec. IV E. Finally, our findings are summarized in Sec. V.

II. MODEL

In this section, we begin by briefly describing the geometrical structure of our system as given in Fig. 1. Figure 1(a) shows the schematic diagram of a TBG where we have rotated the upper layer (layer 2) of an AA-stacked bilayer graphene (where each atom in one layer aligns directly above or below an atom in the other) in an anticlockwise direction by an angle θ with respect to the fixed lower layer (layer 1). The two sublattices in the lower layer are labeled as A_1 (blue) and B_1 (light-blue), while those in the upper layer are A_2 (red) and B_2 (light-red), respectively. The twist center is fixed on a sublattice (A-sublattice) from both layers. The unit cell of a lower layer is spanned by the lattice vectors $\boldsymbol{a}_1 = (1/2, \sqrt{3}/2)a$ and $\boldsymbol{a}_2 = (-1/2, \sqrt{3}/2)a$ as shown in Fig. 1(b). Here, $a = 2.46$ Å is the lattice constant of monolayer graphene and $|\boldsymbol{a}_1| = |\boldsymbol{a}_2| = a$. Alternatively, $\boldsymbol{a}_1'$ and $\boldsymbol{a}_2'$ represent the lattice vectors of the rotated upper layer [66]. Furthermore, the Brillouin zone of the moiré superlattice gets reduced in size with a hexagonal shape when compared to the Brillouin zones of the two separate layers, as shown in Fig. 1(c).

For a commensurate lattice structure within TBG, the lattice vectors in the unit cell can be expressed as $\boldsymbol{a}_1^{(M)} = n\boldsymbol{a}_2 + m\boldsymbol{a}_1$ and $\boldsymbol{a}_2^{(M)} = -m\boldsymbol{a}_2 + (n+m)\boldsymbol{a}_1$, where both m and n are integers. The unit cell of the superlattice contains $N = 4(n^2 + mn + m^2)$ atoms. The rotation angle θ is related to (m, n) by the following condition [31,67]:

$$\cos(\theta) = \frac{m^2 + n^2 + 4mn}{2(m^2 + n^2 + mn)}. \tag{1}$$

For $m = n = 1$ ($m = 1, n = 0$), Eq. (1) reduces to the well-known AA-stacked (AB-stacked) bilayer graphene. This implies that $\theta = 0°$ ($\theta = 60°$) corresponds to the perfect AA-stacking (AB-stacking).

Following Ref. [68], we consider a Hamiltonian consisting of two parts: one is the intralayer part (H_{intra}), and the other is the interlayer part ($H_\perp$). This is true for two or more stacked arrangements of graphene layers. Hence, for a noninteracting system, the tight-binding Hamiltonian can be written in real space as (in the absence of any external field)

$$\begin{aligned} H &= H_{\text{intra}} + H_\perp \\ &= -\sum_{\substack{i\neq j \\ l}} t_{ij}^{ll}(c_{l,i}^\dagger c_{l,j} + \text{H.c.}) \\ &\quad -\sum_{\substack{i,j \\ l\neq l'}} t_{ij}^{l,l'}(c_{l,i}^\dagger c_{l',j} + \text{H.c.}), \end{aligned} \tag{2}$$

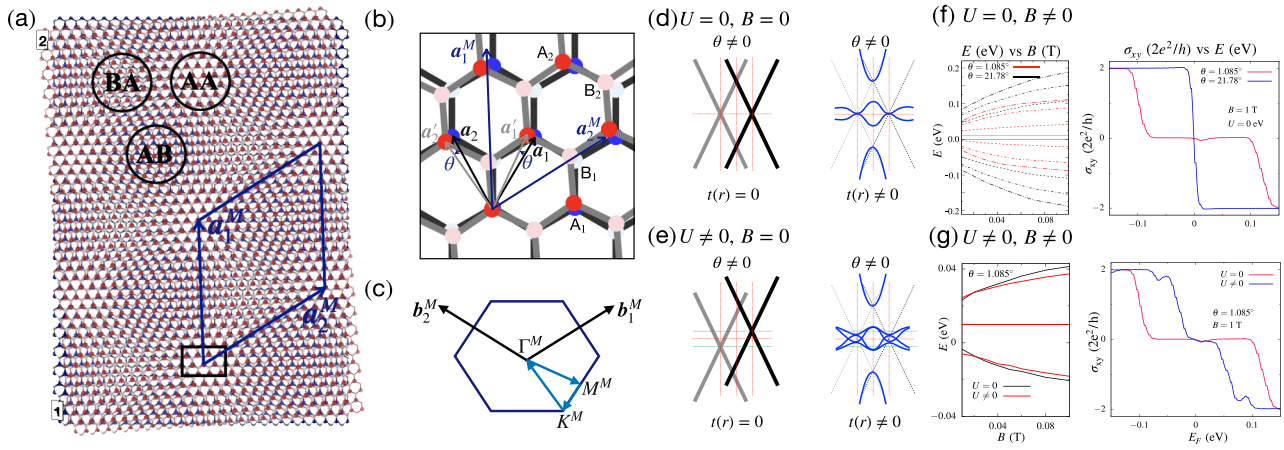

FIG. 1. (a) A schematic diagram of a TBG lattice is shown. The upper layer (denoted as 2) is rotated with respect to the lower layer (denoted as 1) by a certain angle. The three different stacking regions (referred to as AA, AB, and BA) formed in the superlattice structure are outlined by a black circle. (b) An enlarged view of the rectangular box is shown. The two different sublattices in layer 1 are denoted by A_1 (blue) and B_1 (light-blue) and in layer 2 are denoted by A_2 (red) and B_2 (light-red). $\boldsymbol{a}_1$ and $\boldsymbol{a}_2$ are the lattice vectors in layer 1, whereas $\boldsymbol{a}'_1$ and $\boldsymbol{a}'_2$ are the lattice vectors in layer 2. $\boldsymbol{a}^M_1$ and $\boldsymbol{a}^M_2$ are the unit cell lattice vectors for the moiré superlattice. θ corresponds to the rotation angle. (c) The mini Brillouin zone (BZ) of the moiré superlattice in reciprocal space is spanned by the vectors $\boldsymbol{b}^M_1$ and $\boldsymbol{b}^M_2$. The high-symmetry points (Γ^M, K^M, M^M) are given in the Brillouin zone, and the arrows indicate the path over the Brillouin zone. The schematics for band structure is shown without [$t(r) = 0$] and with [$t(r) \neq 0$] interlayer coupling for (d) $U = 0$, $B = 0$, and (e) $U \neq 0$, $B = 0$. For the latter case, when $t(r) = 0$, the uncoupled graphene layers doped to opposite charges under the applied electric field. However, when $t(r) \neq 0$, these layers couple with each other and degeneracy lifted in the low-energy bands at Dirac points in the presence of the applied electric field. Landau levels spectra [E (eV) vs B (T)] and Hall conductivity [σ_{xy} ($2e^2/h$) vs E (eV)] are shown for (f) $U = 0$, $B \neq 0$ with $\theta = 1.085^\circ$ and 21.78°, and (g) $U \neq 0$, $B \neq 0$ with $\theta = 1.085^\circ$. The Landau levels are sensitive to the twist angle and lead to new quantum Hall phases in the system.

where the symbol t^{ll}_{ij} in the first term (H_{intra}) represents the nearest-neighbor intralayer hopping integral between sites i and j. Specifically, t^{ll}_{ij} takes on a value of $V^0_{pp\pi} = 3.09$ eV, which acts at a distance $a_0 = a/\sqrt{3} = 0.142$ nm (a_0 is the carbon-carbon distance of monolayer graphene). $c^\dagger_{l,i}$ and $c_{l,i}$ denote the creation and the annihilation operators, respectively, at site i within layer l. For a simple bilayer case, the layer index l and l' can take values of 1 or 2. H.c. denotes the Hermitian conjugate term. Further, we have not considered any next-nearest-neighbor intralayer hopping terms in H_{intra}.

The second term, denoted as $H_\perp$ in Eq. (2), describes the coupling between layers. For simplicity, we will first explain the term $H_\perp$ for an AB-stacked bilayer graphene. We consider two atoms placed on top of each other and separated by a distance d_0. Then the interlayer hopping integral between these atoms becomes $t(0) = V^0_{pp\sigma} = 0.39$ eV. The on-site energy is set to zero on all atoms. However, in the context of TBG, where the planes are rotated relative to each other, the interlayer hopping integral between sites having an in-plane projection of r and an out-of-plane projection of d_0 can be expressed as follows:

$$t(r) = V^0_{pp\sigma} e^{-\left(\sqrt{r^2+d_0^2}-d_0\right)/\lambda} \frac{d_0^2}{r^2+d_0^2}. \tag{3}$$

As elaborated in Ref. [51], $V_{pp\sigma}$ [$\approx t(r)$] is the dominant factor, but it is adjusted by both the distance and the cosine of the twisted angle. Here, d_0 is taken to be 3.35 Å. λ is the decay parameter that fine-tunes the cutoff of $t(r)$. In our calculations, we adopt a value of $\lambda = 0.27$Å, which effectively reproduces the band structures of simple bilayer graphene without twist.

III. FORMALISM

In this section, we shall describe the numerical method used to compute the transport properties of a TBG system. Our approach is based on a real-space implementation of the Kubo formalism to calculate the dc conductivity of large systems, a technique developed by Garcia *et al.* [69]. The numerical implementation of the kernel polynomial method (KPM) [70,71] entails the expansion of the Bastin formula in terms of Chebyshev polynomials for obtaining the conductivity tensors within the linear-response regime. For noninteracting electrons, the components of the dc conductivity tensor ($\omega \to 0$) [69,72,73] can be expressed using the Kubo-Bastin formula [61,62] as

$$\sigma_{\alpha\beta}(\mu, T) = \frac{ie^2\hbar}{A} \int_{-\infty}^{\infty} d\epsilon f(\epsilon) \text{Tr}\Big\langle v_\alpha \delta(\epsilon - H) v_\beta \frac{dG^+(\epsilon)}{d\epsilon} - v_\alpha \frac{dG^-(\epsilon)}{d\epsilon} v_\beta \delta(\epsilon - H)\Big\rangle, \tag{4}$$

where μ stands for the chemical potential, while T denotes the temperature. The area of the sample is denoted by A. v_α and v_β are the components of the velocity operator for α and β, respectively. $f(\epsilon)$ denotes the Fermi-Dirac distribution function for a given μ and T. $G^\pm(\epsilon, H) = 1/(\epsilon - H \pm i\eta)$ represents the advanced ("−") and the retarded ("+") Green's function, respectively. η is a small positive number ($\eta \to 0^+$).

Using KPM, we can expand the spectral representation of both the rescaled δ and Green's function in terms of Chebyshev polynomials [70]. Consequently, the conductivity tensor

TABLE I. The number of atoms and unit cells used for different twist angles in our system for obtaining magnetotransport properties.

θ (deg)	No. atoms/unit cell	No. unit cells
1.085	11164	(32×32)
2.005	3268	(128×128)
3.890	868	(512×128)
6.009	364	(512×256)
21.78	28	(1024×1024)

[Eq. (4)] can be written as

$$\sigma_{\alpha\beta}(\mu,T)=\frac{4e^2\hbar}{\pi A}\frac{4}{(\Delta E)^2}\int_{-1}^{1}d\tilde{\epsilon}\frac{f(\tilde{\epsilon})}{(1-\tilde{\epsilon}^2)^2}\times\sum_{m,n}\Gamma_{nm}(\tilde{\epsilon})\mu_{nm}^{\alpha\beta}(\tilde{H}), \tag{5}$$

where $\tilde{\epsilon}$ denotes the rescaled energy within the $[-1, 1]$ range. Similarly, $\tilde{H}$ represents the rescaled Hamiltonian, and $\Delta E = E^+ - E^-$ (where E^+ and E^- are the maximum and minimum eigenvalues of the energy spectrum, respectively). The functions $\Gamma_{nm}(\tilde{\epsilon})$ and $\mu_{nm}^{\alpha\beta}(\tilde{H})$ depend on the rescaled energy and Hamiltonian, respectively, and can be expressed as

$$\Gamma_{nm}(\tilde{\epsilon})\equiv(\tilde{\epsilon}-in\sqrt{1-\tilde{\epsilon}^2})e^{in\arccos(\tilde{\epsilon})}T_m(\tilde{\epsilon})+(\tilde{\epsilon}+im\sqrt{1-\tilde{\epsilon}^2})e^{-im\arccos(\tilde{\epsilon})}T_n(\tilde{\epsilon}) \tag{6}$$

and

$$\mu_{nm}^{\alpha\beta}(\tilde{H})\equiv\frac{g_m g_n}{(1+\delta_{n0})(1+\delta_{m0})}\mathrm{Tr}[v_\alpha T_m(\tilde{H})v_\beta T_n(\tilde{H})], \tag{7}$$

where the latter involves the product of Chebyshev polynomial expansions. The Jackson kernel, denoted as g_m, is used to smooth out the Gibbs oscillations [70], which arise due to truncation of the expansion outlined in Eq. (5). $T_m(x)$ is the Chebyshev polynomials, defined by the following recurrence relation:

$$T_m(x)=2xT_{m-1}(x)-T_{m-2}(x), \tag{8}$$

where $T_0(x) = 1$ and $T_1(x) = x$.

The density of states (DOS) can be calculated using the spectral operator $\delta(\tilde{\epsilon}-\tilde{H})$ as

$$\rho(\tilde{\epsilon})=\frac{1}{N}\mathrm{Tr}\delta(\tilde{\epsilon}-\tilde{H})=\frac{1}{\pi\sqrt{1-\tilde{\epsilon}^2}}\sum_{n=0}^{\infty}\mu_n T_n(\tilde{\epsilon}), \tag{9}$$

where μ_n is the Chebyshev moments and is given by

$$\mu_n=\frac{1}{N}\frac{(1+\delta_{n,0})}{2}\mathrm{Tr}\ T_n(\tilde{H}). \tag{10}$$

IV. RESULTS

In the following sections, we will present our numerical results, including the electronic and transport properties of the TBG system. We have simulated a very large system that consists of a number of atoms of the order of 10^7 (ten million). However, since the area of the unit cell depends on the twist angle, the number of unit cells in each system varies. Table I shows the number of atoms and unit cells used in each system for the particular twist angle.

For our analysis, the Chebyshev moments used to expand the Green's function and the Dirac deltas were truncated to $M = 12\,000$ (Chebyshev moments), which is sufficient to attain an energy resolution of the order of ∼1 meV in the DOS spectrum. Also, it is important to note that for the DOS calculations, the number of unit cells considered is even larger compared to Table I. However, for the transport calculation, we used sufficient $M = 6144$ [69] (Chebyshev moments) to avoid the fluctuations in dc Hall conductivity higher-energy plateaus. Nevertheless, it is possible to manipulate the system size and increase the number of Chebyshev moments for very high precision. We have also imposed periodic boundary conditions for all our numerical simulations.

A. Electronic structures (flat bands)

In this section, we mainly focus on the electronic band structure, particularly emphasizing the flat band characteristics of a TBG system near the small twist angles at zero external field. The aim is to illustrate the behavioral transition observed below and above the magic angle in our system. Additionally, we present the DOS plots for the same purpose. In Figs. 2(a)–2(c), we calculate the energy band structures (left)

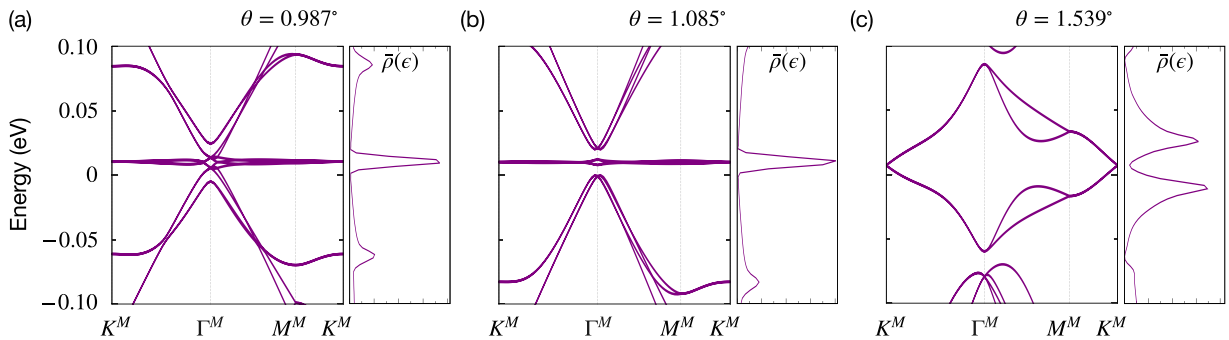

FIG. 2. The electronic band dispersion along the high-symmetry points $K^M \rightarrow \Gamma^M \rightarrow M^M \rightarrow K^M$ [see Fig. 1(c)] and the corresponding normalized density of states, $\bar{\rho}(\epsilon)$, of TBG are shown for (a) $\theta = 0.987^\circ$ and $(m, n) = (34, 33)$, (b) $\theta = 1.085^\circ$ and $(m, n) = (31, 30)$, and (c) $\theta = 1.539^\circ$ and $(m, n) = (22, 21)$, respectively.

and the corresponding normalized DOS, $\bar{\rho}(\epsilon)$ (right), within the low-energy regime for three commensurate small twist angles, $\theta = 0.987^\circ$, 1.085°, and 1.539°, respectively, using Eq. (2). Figure 2(a) shows that the bands are almost flat in the vicinity of charge neutrality when $\theta = 0.987^\circ$. This nearly flat band significantly contributes to the DOS for $\theta = 0.987^\circ$, which can also be seen from Fig. 2(a). The DOS exhibits a prominent sharp peak which corresponds to the flatness of the band dispersion within the low-energy regime, whereas the additional smaller peaks arise due to the saddle points from the remote bands in close proximity to the flat bands. With the tuning of θ, the energy bands exhibit enhanced flatness, leading to the formation of localized states with Fermi velocity close to zero value for $\theta = 1.085^\circ$. This is depicted in Fig. 2(b). At $\theta = 1.085^\circ$, we observe our so-called "magic angle" with two distinct gaps (one above and one below the charge neutrality). However, these gaps are now separated from the remote bands with the reduced bandwidth as compared to $\theta = 0.987^\circ$, where the band overlapping occurs [see Figs. 2(a) and 2(b)]. As a result, the DOS also shows a similar sharp peak near the charge neutrality when $\theta = 1.085^\circ$, but the two other Van Hove peaks that arise from the remote bands are now shifted slightly towards the higher energy as compared to $\theta = 0.987^\circ$ [see Figs. 2(a) and 2(b)]. These flat bands that arise due to the strong interlayer coupling also have implications in the LL spectra, which are discussed later in Sec. IV C.

Above the magic angle (when $\theta = 1.539^\circ$), the flatness of the band near the charge neutrality almost vanishes and becomes dispersive within the same energy range, especially near the Γ^M point in the BZ [see Fig. 2(c)]. The corresponding DOS reveals the presence of two diverging Van Hove singularities located near the charge neutrality. However, the separation between these two singularities increases as the twist angle continues to increase [74]. It is important to note that the energy spectrum as well as the DOS are not symmetrical with respect to zero energy for small twist angles, as shown in Fig. 2. Hence, we observe a small shift in the charge neutrality due to the broken particle-hole symmetry of the model at small twist angles.

B. Effects of an external electric field

In this section, we discuss the effects of an external electric field (which breaks the inversion symmetry) on the electronic properties of the TBG system at $\theta = 0.987^\circ$, 1.085°, and 1.539°. To introduce a perpendicular electric field, we apply an electric field strength of $+U/2$ on layer 1 (lower) and $-U/2$ on layer 2 (upper). In Fig. 3, we show how the energy band structures and the normalized density of states, $\bar{\rho}(\epsilon)$, depend on the electric field strength difference between the two layers with a small twist and also evolve with the tuning of the electric field strength. It is well known that the Dirac cone touching is protected by the C_2T (time-reversal) symmetry and can be gapped out by breaking this symmetry. In the case of a TBG system, the external electric field does not induce a band gap in the spectrum protected by the C_2 (180°) rotational symmetry [37]. Nevertheless, it does facilitate the transfer of electronic charge from the lower layer to the upper layer of the system [75]. This excess electronic charge has a strong variation for small twist angles.

In the absence of an external electric field, the two bands (namely, the lowest conduction band and the highest valence band) across the charge neutrality touch each other at the superlattice Dirac point labeled as K^M (see Fig. 2). When an electric field is introduced, the degeneracy of the two layers (upper and lower layers) at the K^M point is lifted due to different on-site energies induced in each layer. As a consequence, the two Dirac points move in opposite directions in energy, and lift the degeneracy with an energy shift at the K^M point of the moiré BZ. We denote it as $\Delta E(K^M)$. We also find that the DOS peaks get broadened and eventually the singularity in DOS vanishes with the increasing field. Figure 3(a) illustrates the band structures as well as the DOS at $U = 0.2$ eV for $\theta = 0.987^\circ$ (left panel), 1.085° (middle panel), and 1.539° (right panel), respectively. The flatness behavior of the energy bands near the charge neutrality observed for the $U = 0$ case is now reduced with the lifting degeneracy, resulting in broadened peaks in the DOS. The broadening is a consequence of a dispersive splitting in the flat bands for $U \neq 0$. This phenomenon is evident in Fig. 3(a) for $\theta = 0.987^\circ$ and 1.085°, respectively. Additionally, the gap above and below the charge neutrality is no longer observed for $\theta = 1.085^\circ$ in the presence of the electric field. However, this effect is negligible for $U = 0.2$ eV when $\theta = 1.539^\circ$, as shown in the right panel of Fig. 3(a). When the strength of the electric field, U, is increased from 0.2 to 0.4 eV, the band dispersion and the corresponding DOS start evolving in a peculiar fashion below a certain θ value. The energy difference within the Van Hove singularity peaks in the DOS around the charge neutrality diminishes as the flat bands disappear with increasing bandwidth, as depicted in Fig. 3(b). As we further increase the value of U (say, $U = 0.6$ eV), we observe the significant contribution from the remote bands especially near the charge neutrality where the bands are dispersive in nature [see Fig. 3(c)]. Also, the merging of the VHS peaks is observed in the corresponding DOS spectrum [see Fig. 3(c)]. This underscores the possibility of controlling the position of both the charge neutrality and the VHS by varying the twist angle and gate voltage, respectively. This offers a potent toolkit for manipulating the electronic states of the system.

For clarity of our findings, we further investigate the tunability of energy shift at the K^M point, denoted as $\Delta E(K^M)$ as a function of both rotation angle, θ, and the electric field strength, U. In Fig. 4(a), we have shown the energy difference, $\Delta E(K^M)$, while varying the twist angle, θ, for $U = 0.2$, 0.4, and 0.6 eV. Interestingly, $\Delta E(K^M)$ remains almost constant for a certain range of θ ($\theta > 10^\circ$) across all the values of U by converging to the magnitude equal to the applied electric field strength, and subsequently exhibits a steep decline for $\theta < 10^\circ$. Nonetheless, this feature becomes particularly remarkable at extremely small twist angles depending on the values of the external electric field, as depicted in Fig. 4(b) with a zoomed view. For the previous case ($\theta > 10^\circ$), the shift occurs at $+U/2$ for layer 1 in the positive energy and at $-U/2$ for layer 2 in the negative energy due to the weak interlayer coupling near the charge neutrality where the layers behave as decoupled. However, for the latter case, we observe multiple closing and reopening of the energy shift at the K^M point approximately for $\theta < 3^\circ$ since the energy levels disperse nonmonotonically with the variation of the electric field

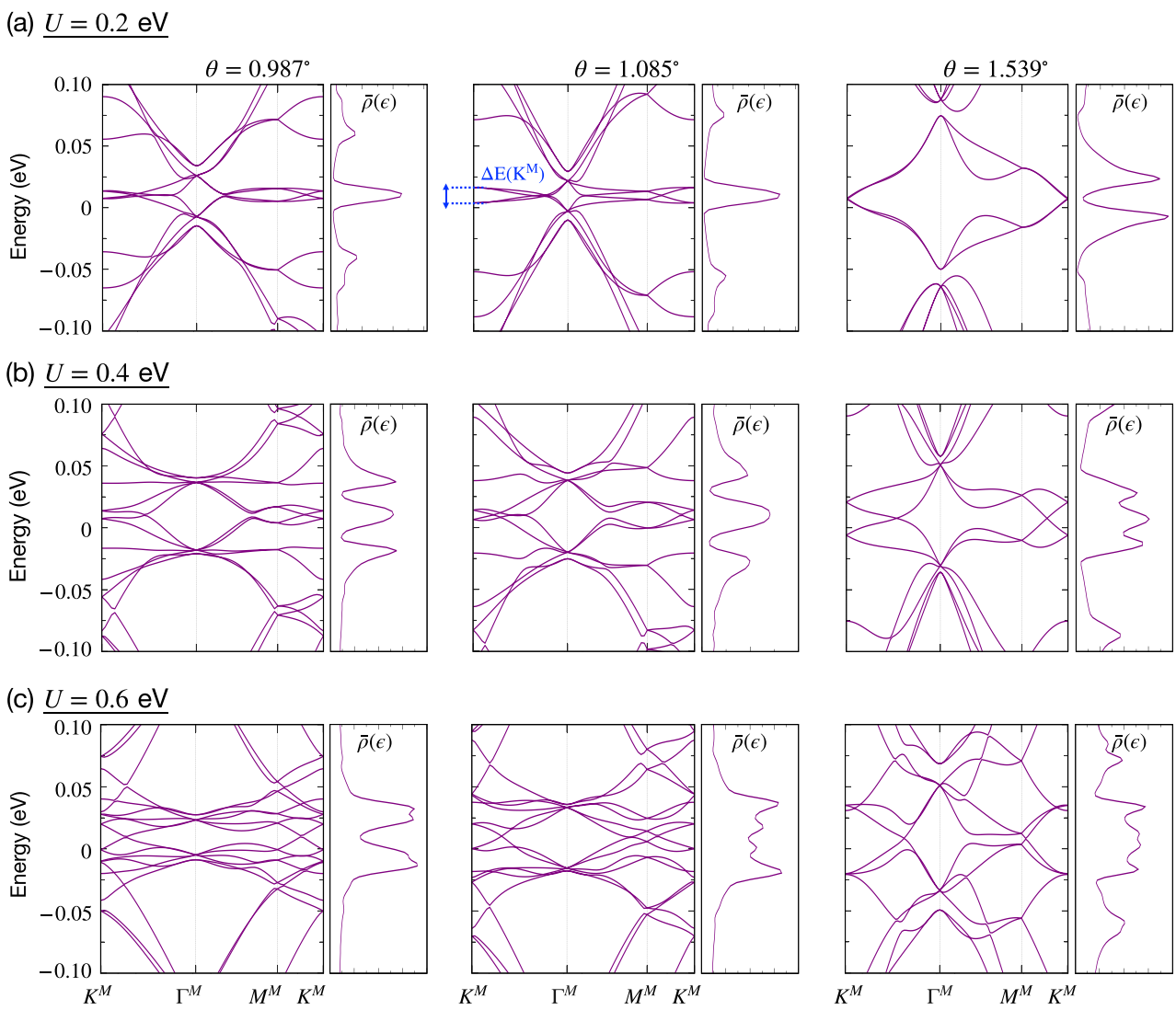

FIG. 3. The electronic band dispersion along the high-symmetry points $K^M \rightarrow \Gamma^M \rightarrow M^M \rightarrow K^M$ and the corresponding normalized density of states, $\bar{\rho}(\epsilon)$, of TBG are shown for (a) $U = 0.2$ eV, (b) $U = 0.4$ eV, and (c) $U = 0.6$ eV with $\theta = 0.987°$ and $(m, n) = (34, 33)$ (in the left panel), $\theta = 1.085°$ and $(m, n) = (31, 30)$ (in the middle panel), and $\theta = 1.539°$ and $(m, n) = (22, 21)$ (in the right panel), respectively. The shift in energy at the Dirac point, $\Delta E(K^M)$, is denoted by the blue dotted lines.

strength in this regime. At low field strength ($U = 0.2$ eV), this anomalous behavior of the energy shift manifests below 1.6° (indicated by the black curve), whereas for the other two values, $U = 0.4$ and 0.6 eV, the same phenomenon occurs below 1.8° (indicated by the blue curve) and 2.4° (indicated by the brown curve), respectively. Figure 4(c) shows the plot for $\Delta E(K^M)$ as a function of U when $\theta = 1.085°$. The nonmonotonic behavior in $\Delta E(K^M)$ is still observed with a similar energy shift closing and reopening while varying the field strength U.

C. Effects of the magnetic field

In this section, we shall explore the effects of a magnetic field applied perpendicular to the plane of a TBG system in the absence of an external electric field. We consider a uniform magnetic field $\vec{B} = B\hat{z}$, where B represents the strength of the magnetic field. The magnetic flux per unit cell is defined as $\phi = BS$ (S being the area of TBG unit cell), measured in units of the flux quantum $\phi_0 = h/e$. We incorporate the magnetic field effect by multiplying the Peierls phase factor $e^{2i\pi\phi_{ij}}$ (where ϕ_{ij} is the magnetic flux) into the hopping terms [as outlined in Eq. (2)] using the Peierls substitution method [76–78]. It is important to note that, in contrast to a conventional superlattice, the strength of the magnetic field, B, in a TBG system is determined by the size of the unit cell. As the dimensions of the unit cell increase, the necessary strength of the magnetic field decreases. Consequently, with smaller twist angles, which correspond to larger unit cell dimensions, a weaker magnetic field is sufficient to quantize the single-particle electronic states into LLs [79]. In Fig. 5(a), we calculate the density of states, $\rho(\epsilon)$, as a function of energy, E, for different values of B with $\theta = 1.085°$. At a very low magnetic field $B = 0.01$ T [which corresponds to magnetic flux per unit cell $(\phi/\phi_0) \approx 0.000\ 35$], the discreteness of the LL peaks is very small. However, as we increase the

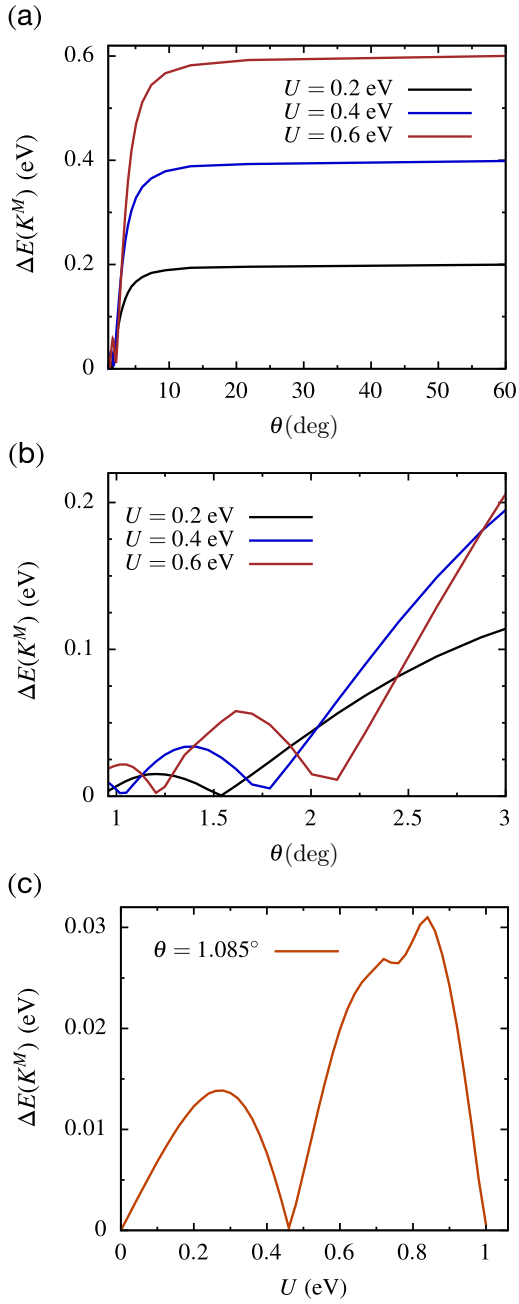

FIG. 4. (a) Energy shift, $\Delta E(K^M)$ (in units of eV), is shown as a function of twist angles, θ (in units of degree), for $U = 0.2$, 0.4, and 0.6 eV (b) Zoomed view of $\Delta E(K^M)$ near the small twist angle ($1° \leqslant \theta \leqslant 3°$) is shown. (c) Energy shift, $\Delta E(K^M)$ (in units of eV), is shown as a function of electric field strength, U (in units of eV), at $\theta = 1.085°$.

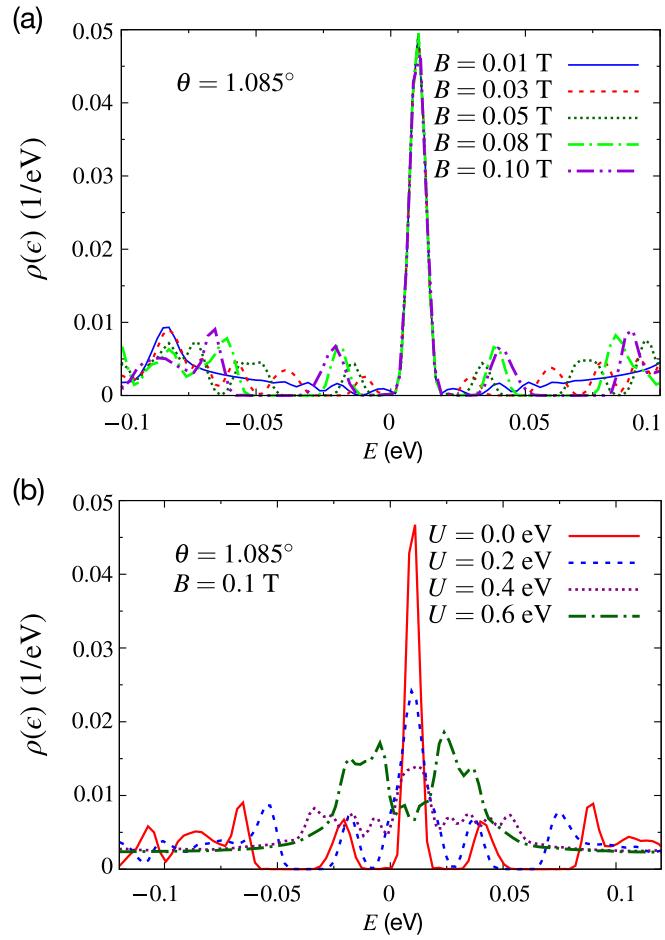

FIG. 5. (a) The density of states, $\rho(\epsilon)$ (in units of 1/eV), is shown as a function of energy, E (in units of eV), for different values of B at $\theta = 1.085°$. (b) The density of states, $\rho(\epsilon)$ (in units of 1/eV), is plotted as a function of energy, E (in units of eV), for different values of electric field strength, $U = 0.0$, 0.2, 0.4, and 0.6 eV, at a fixed value of B ($B = 0.1$ T) when $\theta = 1.085°$.

magnetic field value B, the LL peaks become more pronounced. Nevertheless, only a few LLs can be clearly distinguished away from the charge neutrality for $\theta = 1.085°$, even in the case of a larger B value [say $B = 0.1$ T, that corresponds to magnetic flux per unit cell $(\phi/\phi_0) \approx 0.0035$], which is not true for large twist angles. The influence of the higher LLs is overridden by those originating from the band edge. Most importantly, the DOS near the charge neutrality, corresponding to the flat band, is independent of the strength of the magnetic field since it has topological protection [50]. In the DOS plot [Fig. 5(a)], the peak at charge neutrality is not a Landau level but arises from the unaltered flat band due to strong C3 symmetry preservation. Furthermore, we illustrate the Landau level energies, labeled as E, as a function of the magnetic field B for a range of twist angles, namely 1.085°, 2.005°, 3.89°, and 21.78° within the low magnetic field regime and at low energies. These results are depicted in Fig. 6(a). When the twist angle is sufficiently large (as in the case of $\theta = 21.78°$), the low-energy LL spectrum behaves similarly to monolayer graphene, with a dependence on both n ($n > 0$) and B following a square-root relationship. This suggests that, at lower energies, interlayer couplings are relatively weak. However, as we reduce the twist angle, for example, to $\theta = 3.89°$ and 2.005°, we still observe similar structures resembling the Landau levels of monolayer graphene in the low-energy LL spectra (below 0.2 eV), albeit with variations in the energy scale. When the twist angle becomes even smaller, as in the case of a magic angle ($\theta = 1.085°$), the low-energy LL spectra become compressed near the Dirac points. This behavior is consistent with the observed reduction in

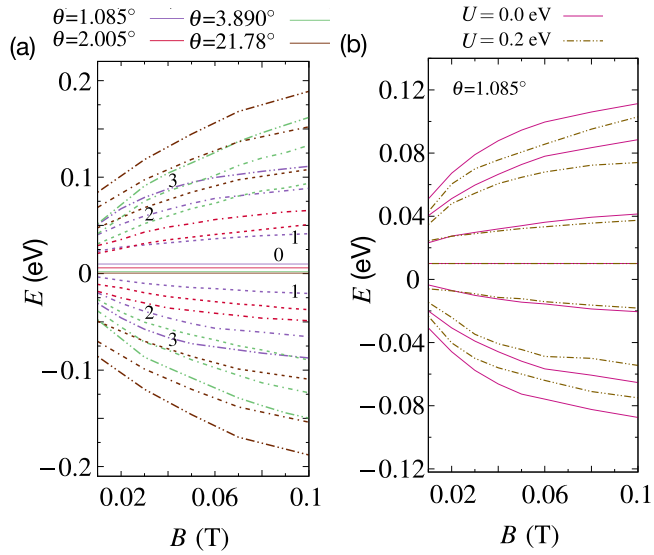

FIG. 6. (a) Landau level energies, E (in units of eV), are plotted as a function of the magnetic field strength, B (in units of T), for different twist angles, $\theta = 1.085°, 2.005°, 3.890°, 21.78°$, as indicated by the different colors. The solid lines indicate the zero-mode energy states for all the twist angles. $n = 1, 2, 3$ denotes the three lowest Landau levels with index n for $\theta = 1.085°$. (b) Landau level energies, E (in units of eV), are shown as a function of the magnetic field strength, B (in units of T), for $U = 0$ and 0.2 eV at $\theta = 1.085°$.

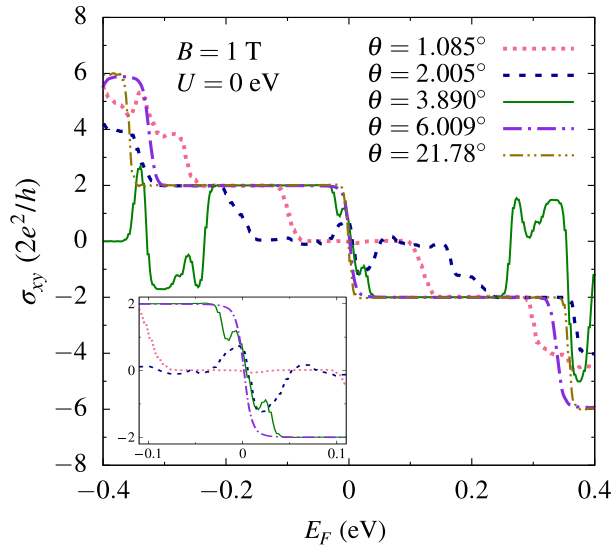

FIG. 7. Hall conductivity, σ_{xy} (in units of $2e^2/h$), is shown as a function of Fermi energy, E_F (in units of eV), for different twist angles, namely $\theta = 1.085°$, $2.005°$, $3.89°$, $6.009°$, and $21.78°$ for $B = 1$ T and $U = 0$ eV. The inset shows the zoomed view around $E_F = 0$.

bandwidth for smaller twist angles due to significant interlayer coupling, in contrast to larger twist angles. However, the zero energy level remains unaltered, which is true for all the twist angles [see Fig. 6(a)]. Additionally, the zero energy peaks shift towards positive energies (electron side) as θ decreases. There are energy level crossings as a function of the magnetic field for various twist angles within this low field regime. However, the energy difference between the zeroth LL to the higher-energy LLs decreases with the twist angle. Moreover, when the Landau level energy falls below the Van Hove energy (0.1 eV), energy levels exhibit eightfold degeneracy (spin, valley, and layers degree of freedom) at very low magnetic fields, reducing to fourfold degeneracy at higher fields.

D. Effects of both electric field and magnetic field

In this section, we explore the influence of an external perpendicular electric field, U, on the LL spectra in a TBG system at low magnetic fields. We first observe how the LL peaks get modified while varying the strength of the electric field. Figure 5(b) shows the DOS, $\rho(\epsilon)$, as a function of energy, E, at low B field ($B = 0.1$ T) for $U = 0$, 0.2, 0.4, and 0.6 eV with $\theta = 1.085°$. Within the low-energy range, we observe a reduction in the number of LL peaks with the increase of the electric field strength, as these LLs are pushed to a higher energy range. Eventually, at a critical electric field strength ($\sim$ 0.6 eV), no $n > 0$ LL peaks appear for energy range $\pm$ 0.1 eV as shown in Fig. 5(b). Consequently, it becomes possible to achieve electrically adjustable LL spectra in TBG. Figure 6(b) shows the Landau level energies, E, as a function of the magnetic field, B, under an electric field strength of $U = 0.2$ eV. For the sake of comparison, we have also shown the Landau level energies corresponding to the case when $U = 0$ eV. Notably, the zero energy peak remains unchanged for both scenarios, i.e., for $U = 0$ eV and $U \neq 0$ eV. However, the higher energy LLs ($n > 0$) exhibit a discernible shift towards low energy for the $U \neq 0$ case, as indicated by the dotted lines in Fig. 6(b). Moreover, we observe the energy level crossings in the LL spectra at very low energies.

E. Hall conductivity

In this section, we investigate the transport properties of the TBG system in terms of the Hall conductivity, denoted as σ_{xy}, with respect to the Fermi energy, E_F, for different twist angles using Eq. (4) as elaborated in Sec. III. In Fig. 7, we have plotted σ_{xy} as a function of Fermi energy, E_F, for $\theta = 1.085°$, $2.005°$, $3.89°$, $6.009°$, and $21.78°$ with $U = 0$ eV and $B = 1$ T at absolute zero temperature. The Hall conductivity σ_{xy} exhibits a sequence of quantized plateaus for all the twist angles but with a significant difference in the quantized value of σ_{xy}. More precisely, as we tune the twist angle from a larger value to a smaller one, a critical point emerges around $\theta = 2.005°$ where σ_{xy} shifts from a half-integer to an integer quantum Hall effect, i.e., the value of σ_{xy} shifts from $\pm 4(n + 1/2)$ $(2e^2/h)$ to $\pm 2n$ $(2e^2/h)$, n being the integers (2 in front of e^2/h is accounted for spin degeneracy). This is depicted in the inset of Fig. 7. For a very large twist angle (when $\theta = 21.78°$), σ_{xy} follows a well-established sequence $\pm 2, \pm 6, \pm 10, \ldots$ in units of $2e^2/h$ which is double that of a monolayer graphene [46]. The underlying reason is obvious, i.e., the two layers behave as a decoupled layer, implying that the Landau level spectra are almost equivalent to the monolayer's LL. Moreover, due to the layer degeneracy, we see that the Hall conductivity in steps of $8e^2/h$ between each plateau in σ_{xy} indicates the presence of eightfold (layer, valley, and spin) degeneracy of the LL. Although the Hall conductivity follows the same sequence for $\theta = 6.009°$ as already observed for $21.78°$, the behavior is

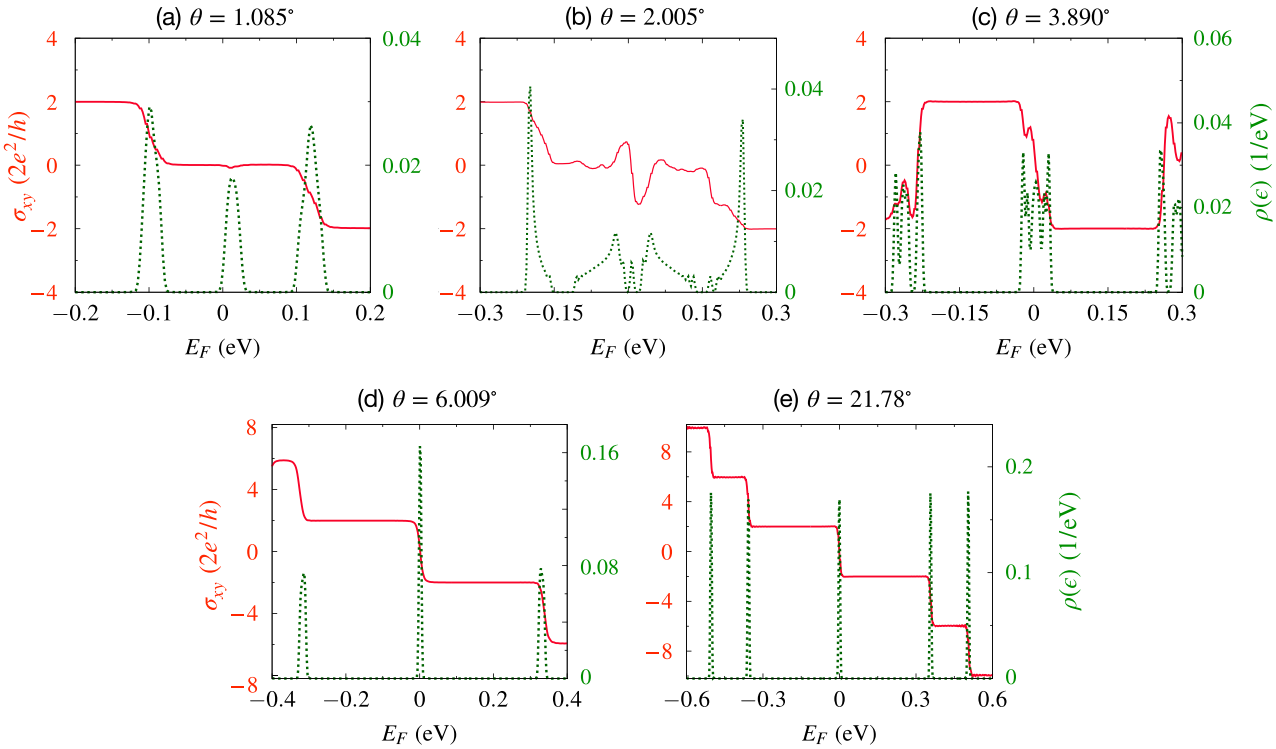

FIG. 8. Hall conductivity, σ_{xy} (in units of $2e^2/h$), is plotted as a function of Fermi energy, E_F (in units of eV), and their corresponding density of states, $\rho(\epsilon)$ (in units of $1/\text{eV}$), is shown for (a) $\theta = 1.085°$, (b) $\theta = 2.005°$, (c) $\theta = 3.089°$, (d) $\theta = 6.009°$, and (e) $\theta = 21.78°$ with $U = 0$ eV and $B = 1$ T.

different for $\theta = 3.89°$ due to the complicated structure in the LL spectra [see Fig. 8(c)]. At $\theta = 3.89°$, the Hall conductivity exhibits distinct quantized plateaus, while we go to the higher energy regime. Specifically, it turns negative (-2 in units of e^2/h) on the hole side and positive ($+2$ in units of e^2/h) on the electron side. Additionally, a zero-energy plateau emerges with further tuning of the Fermi energy [51]. As we further reduce the twist angle to a lower value ($\theta = 2.005°$), the system undergoes a transition where a zero energy plateau emerges near the Dirac point with small fluctuations. Moreover, the Hall plateaus follow a different sequence as 0, ± 2, ± 4, ± 6, … in units of $2e^2/h$. Similarly, at the magic angle ($\theta = 1.085°$), the Hall plateaus follow the same sequence as observed for $\theta = 2.005°$ except for the fluctuations near the zero Fermi energy. Interestingly, for the smaller twist angles ($1.085°$ and $2.005°$), the coupled layers show that the Hall conductivity in steps of $4e^2/h$ between each plateau in σ_{xy} indicate the presence of fourfold (valley and spin) degeneracy. The crossover between the Hall conductivity quantization sequence indicates that, for twist angles less than $\theta = 3.890°$, the interlayer coupling spreads over the long periodic cells, which is responsible for the flat bands, precisely localization of carriers or massive electrons change the transport of the carriers. Above the twist angles $\theta = 3.890°$ the transport is similar to the massless Dirac fermions [46].

In Figs. 8(a) and 8(e), we demonstrate the behavior of the LL peaks, denoted as $\rho(\epsilon)$ (green curve) during the transition of Hall conductivity, σ_{xy} (red curve), from one plateau to another for every value of θ as illustrated in Fig. 7. Interestingly, we observe that although there is a sharp plateau near the zero Fermi energy at $\theta = 1.085°$, a zero energy peak still exists in the DOS spectrum [Fig. 8(a)]. This zero-energy peak mainly arises from the flat band due to strong C3 symmetry preservation. However, for $\theta = 2.005°$, we observe an increased number of LL peaks near the zero Fermi energy which is supported by the nondiscrete behavior of the quantized Hall plateau, as can be seen from Fig. 8(b). The quantization happens at $\pm 2n$ $(2e^2/h)$ for both twist angles. These LL spectra become complicated for $\theta = 3.890°$, which shows several LL peaks during the transition from one plateau to another [Fig. 8(c)]. Nevertheless, with increasing value of θ, we observe changes in the quantization of the Hall plateaus, which is also supported by the LL spectra for each of the cases [see Figs. 8(d) and 8(e)]. The presence of a zero energy LL peak indicates the absence of a zero energy Hall plateau for both cases, i.e., for $\theta = 6.009°$ and $21.78°$. We also observe that the energy range required to accommodate the LL peaks increases as we increase the θ value (see Fig. 8). Moreover, the width of these plateaus associated with the LL transitions depends on the gap between the two consecutive LLs in the DOS spectra.

Weak and strong magnetic fields: Next, we discuss the effects of weak as well as strong magnetic fields on the Hall conductivity with $U = 0$ as illustrated in Fig. 9. As we know, the Hall conductivity depends on the available LLs in the given energy range, and these LLs can be controlled with the strength of the applied magnetic field. Also for the case of TBG, the magnetic field is found to be an effective control knob besides the twist angle to change the Hall conductivity. In Fig. 9(a), we have shown the evolution of σ_{xy} as a function of Fermi energy, E_F, and the density of states [$\rho(\epsilon)$] for the

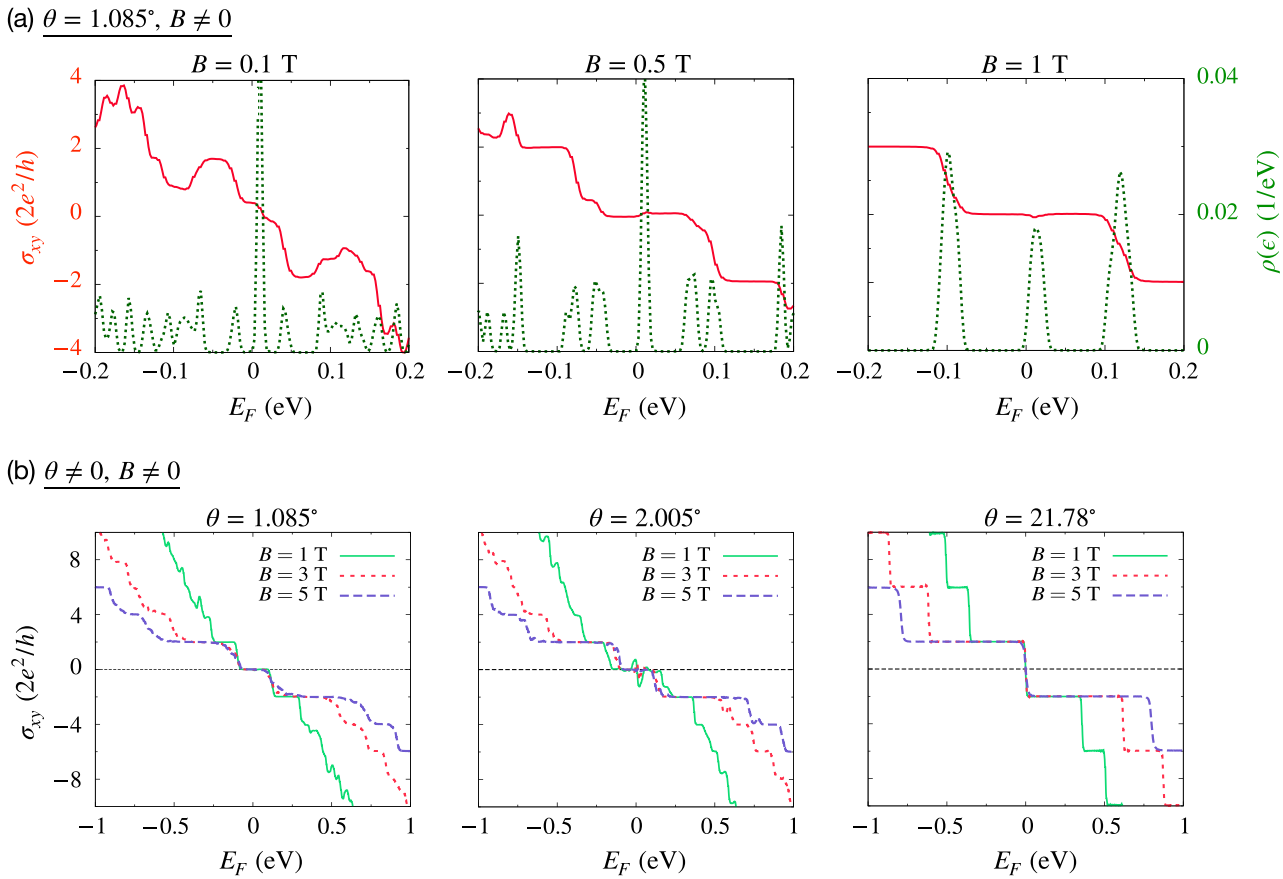

FIG. 9. (a) Hall conductivity, σ_{xy} (in units of $2e^2/h$), is plotted as a function of Fermi energy, E_F (in units of eV), and their corresponding density of states, $\rho(\epsilon)$ (in units of 1/eV), is shown for $B = 0.1$, 0.5, and 1 T with $U = 0$ eV and $\theta = 1.085°$. (b) Hall conductivity σ_{xy} (in units of $2e^2/h$) is plotted as a function of Fermi energy, E_F (in units of eV), for different values of B for $\theta = 1.085°$, 2.005°, and 21.78° with $U = 0$ eV.

weak magnetic field B with $\theta = 1.085°$ within the low-energy range. It can be seen that the zero energy peak exists in the DOS spectra for all values of B arising from the flat band characteristic. However, this zero energy peak does not contribute to the Hall conductivity, and consequently a Hall plateau is present near the zero Fermi energy. At a very low magnetic field (e.g., $B = 0.1$ T), the Hall quantization values exhibit a nondiscrete behavior, as can be seen from Fig. 9(a). Nonetheless, the overall shape of the plateau transitions corroborates with the characteristics of the LL peaks. Upon increasing the strength of the B field ($B = 0.5$ T), the discreteness of the Hall plateaus becomes evident and gets even more pronounced when $B = 1$ T [see Fig. 9(a)]. In Fig. 9(b), we have shown the effects of strong magnetic fields (which is up to 5 T) on the Hall conductivity σ_{xy} for $\theta = 1.085°$, 2.005°, and 21.78°. In the case of a strong B field, the Hall plateaus become sharper with increasing B field. Furthermore, the width of these plateaus varies with increasing magnetic field strength B for all the twist angles ($\theta = 1.085°$, 2.005°, and 21.78°). Additionally, it can be seen that the Hall plateaus exhibit some fluctuations away from the zero Fermi energy at higher energies for $\theta = 1.085°$ and 2.005°, which is absent for $\theta = 21.78°$. However, these artifacts can be improved with a higher truncation order of the expansion and by considering a larger sample size for the former case.

Effects of electric fields: Further, we see the effects of the electric field on the Hall conductivity for $\theta = 1.085°$, 2.005°, and 21.78° with $U \neq 0$ at a fixed B value as shown in Fig. 10. As discussed in Sec. IV B, the low energy bands are strongly influenced in the presence of external electric fields; it will be interesting to see the changes in Hall conductivity with the nonzero applied electric field for the TBG. In Fig. 10(a), we have shown the Hall conductivity σ_{xy} as a function of Fermi energy E_F and the density of states $[\rho(\epsilon)]$ for $\theta = 1.085°$, 2.005°, and 21.78° with $U = 0.2$ eV and $B = 1$ T. In the presence of an electric field, the Hall conductivity shows a similar quantization rule (0, ±2, ±4, ±6, ... in units of $2e^2/h$), as observed previously for the $U = 0$ case for $\theta = 1.085°$ and 2.005° [see Fig. 10(a)]. The LL peaks show splitting for $\theta = 1.085°$ while σ_{xy} makes a transition from one plateau to another within the low energy range as shown in Fig. 10(a). Moreover, the splitting is also observed in the DOS spectra even when $\sigma_{xy} = 0$ due to the broken layer degeneracy. Similarly, for $\theta = 2.005°$, the LL peak splitting is still there in the DOS spectra when $\sigma_{xy} = 0$ as shown in Fig. 10(a). However, when $\theta = 21.78°$, we observe the emergence of new plateaus in addition to the existing ones in the Hall conductivity phenomenon, resulting in an increased number of LL peaks within the same energy range. Hence, the Hall quantization follows a different sequence as 0, ±2, ±4, ±6, ... in units

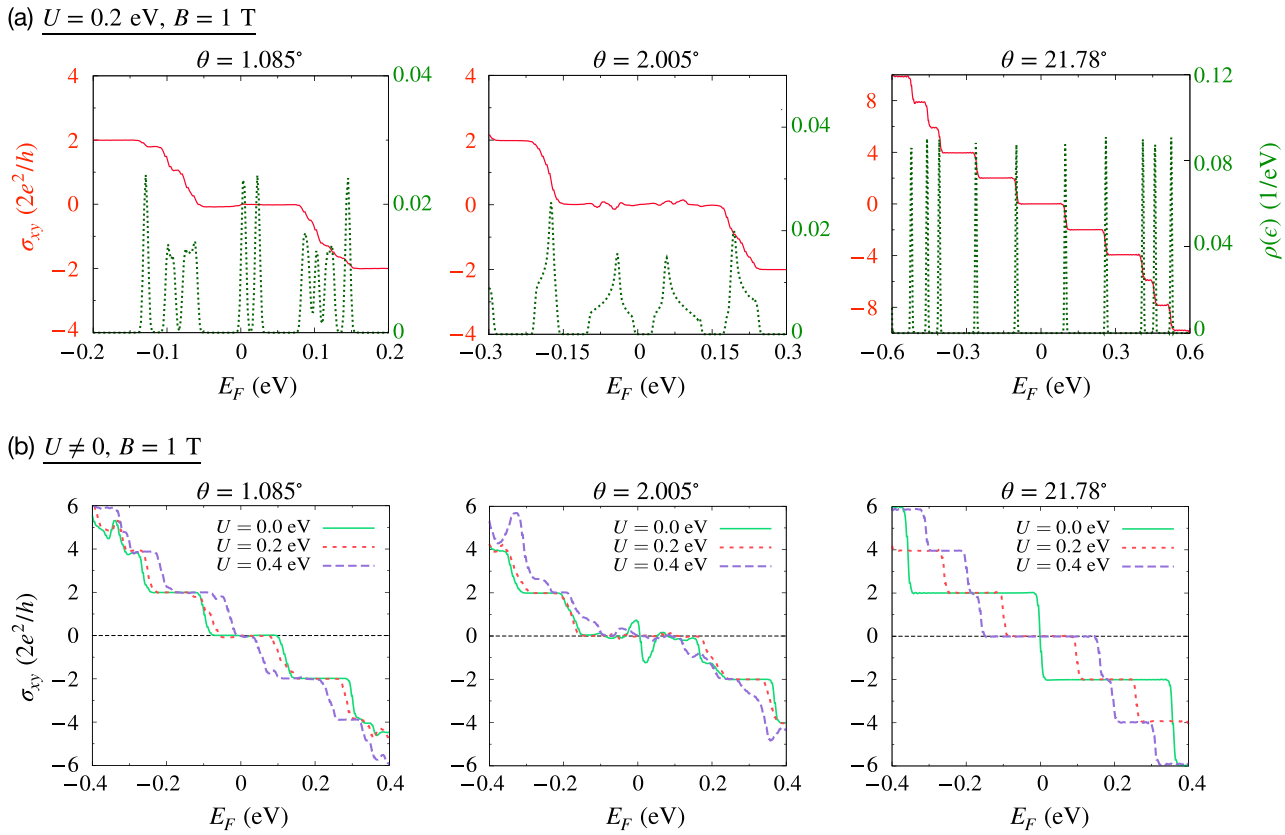

FIG. 10. (a) Hall conductivity, σ_{xy} (in units of $2e^2/h$), is plotted as a function of Fermi energy, E_F (in units of eV), and their corresponding density of states, $\rho(\epsilon)$ (in units of 1/eV), is shown for $\theta = 1.085°$, $2.005°$, and $21.78°$ with $B = 1$ T and $U = 0.2$ eV. (b) Hall conductivity, σ_{xy} (in units of $2e^2/h$), is plotted as a function of Fermi energy, E_F (in units of eV), for different values of U for $\theta = 1.085°$, $2.005°$, and $21.78°$ with $B = 1$ T.

of $2e^2/h$ as compared to the $U = 0$ case [see Fig. 10(a)]. These steps of $4e^2/h$ between each plateau in σ_{xy} indicate the presence of fourfold (valley and spin) degeneracy of the LL for $U \neq 0$. This Hall conductivity plateau, which exists at zero Fermi energy, also supports the absence of zero energy LL. Further, we show similar plots by varying the electric field strengths $U = 0$, 0.2, and 0.4 eV for a fixed B value ($B = 1$ T) in Fig. 10(b). For $\theta = 1.085°$ and $2.005°$, the width of the Hall plateau near the zero Fermi energy decreases with the increasing electric field strength, which remains the same with increasing value of the applied magnetic field [see Figs. 9(b) and 10(b)]. For the latter case, the nondiscrete behavior near the zero Fermi energy vanishes when $U = 0.4$ eV. However, for $\theta = 21.78°$, the width of the Hall plateau near the zero Fermi energy increases with the increasing electric/magnetic field strength as compared to the other two twist angles.

V. CONCLUSIONS

In summary, we have studied the electronic and transport properties under the influence of external electric and magnetic fields employing a tight-binding model for a TBG system. In the absence of an external field, the energy bands of TBG near the Fermi level exhibit a flat nature, leading to the localization of electronic states for small twist angles falling within the range of $0.985° < \theta < 1.539°$. However, when we apply the electric field, the degeneracy at the superlattice Dirac point (K^M) gets lifted, and the $\Delta E(K^M)$ at the Dirac point behaves nonmonotonically with the variation of twist angles, $\theta < 3°$. This suggests that the electric field can be used as an effective tool to manipulate the electronic band structure in the proximity of the flat band region. Next, we explore how the LLs spectra behave for different twist angles in a weak magnetic field. Moreover, we have demonstrated the behaviors of the LLs spectra in the presence of an electric field. We observe a reduction in the number of LL peaks with the increase of the electric field strength within the low-energy regime, as these LLs are pushed to a higher energy range. Additionally, we have found that the Hall quantization rules depend on the twist angle. At small twist angles ($\theta = 1.085°$ and $2.005°$), the Hall plateaus follow a different sequence as 0, ± 2, ± 4, ± 6, … in units of $2e^2/h$ as compared to the larger twist angle ($\theta = 21.78°$). Interestingly, at small angles, the electric field effect does not change the Hall quantization, which is highly in contrast to the large twist angle. At small twist angles (for $\theta = 1.085°$ and $2.005°$), the width of the plateau near the zero Fermi energy decreases as we increase the electric field strength, while it remains the same with the increasing B field. However, for large θ, the width of the plateau near the zero Fermi energy increases as we increase the electric or magnetic field strength. This study opens up an opportunity for deciphering the interplay between the external

fields and the twisting effect on the TBG, uncovering the rich physics of TBG in the presence of uniform electric and magnetic fields. Moreover, it will contribute to the experimental investigations of magic angles with flat bands.

ACKNOWLEDGMENTS

The authors acknowledge the support provided by the KEPLER computing facility, maintained by the Department of Physical Sciences, IISER Kolkata. P.S. and A.M. acknowledge the financial support from IISER Kolkata through the Institute Post-doctoral and PhD Fellowship, respectively. S.M.J. acknowledges funding from the Royal Society through a Royal Society University Research Fellowship URFR191004. B.L.C. acknowledges the SERB for Grant No. SRG/2022/001102 and "IISER Kolkata Start-up-Grant" Ref. No. IISER-K/DoRD/SUG/BC/2021-22/376.

[1] P. R. Wallace, Phys. Rev. **71**, 622 (1947).
[2] A. H. Castro Neto, F. Guinea, N. M. R. Peres, K. S. Novoselov, and A. K. Geim, Rev. Mod. Phys. **81**, 109 (2009).
[3] A. K. Geim and K. S. Novoselov, Nat. Mater. **6**, 183 (2007).
[4] A. K. Geim and I. V. Grigorieva, Nature (London) **499**, 419 (2013).
[5] J. M. B. Lopes dos Santos, N. M. R. Peres, and A. H. Castro Neto, Phys. Rev. Lett. **99**, 256802 (2007).
[6] R. Bistritzer and A. H. MacDonald, Proc. Natl. Acad. Sci. USA **108**, 12233 (2011).
[7] A. O. Sboychakov, A. L. Rakhmanov, A. V. Rozhkov, and F. Nori, Phys. Rev. B **92**, 075402 (2015).
[8] E. Y. Andrei and A. H. MacDonald, Nat. Mater. **19**, 1265 (2020).
[9] K. Kim, A. Walter, L. Moreschini *et al.*, Nat. Mater. **12**, 887 (2013).
[10] E. J. Mele, Phys. Rev. B **84**, 235439 (2011).
[11] R. Bistritzer and A. H. MacDonald, Phys. Rev. B **84**, 035440 (2011).
[12] Z.-D. Chu, W.-Y. He, and L. He, Phys. Rev. B **87**, 155419 (2013).
[13] G. Li, A. Luican, J. M. B. Lopes dos Santos, A. H. Castro Neto, A. Reina, J. Kong, and E. Y. Andrei, Nat. Phys. **6**, 109 (2010).
[14] D. L. Miller, K. D. Kubista, G. M. Rutter, M. Ruan, W. A. de Heer, M. Kindermann, P. N. First, and J. A. Stroscio, Nat. Phys. **6**, 811 (2010).
[15] K. Hermann, J. Phys.: Condens. Matter **24**, 314210 (2012).
[16] W. Yan, M. Liu, R.-F. Dou *et al.*, Phys. Rev. Lett. **109**, 126801 (2012).
[17] J. Hass, W. A. de Heer, and E. H. Conrad, J. Phys.: Condens. Matter **20**, 323202 (2008).
[18] M. Sprinkle, D. Siegel, Y. Hu, J. Hicks, A. Tejeda, A. Taleb-Ibrahimi, P. LeFevre, F. Bertran, S. Vizzini, H. Enriquez, S. Chiang, P. Soukiassian, C. Berger, W. A. de Heer, A. Lanzara, and E. H. Conrad, Phys. Rev. Lett. **103**, 226803 (2009).
[19] X. Li, W. Cai, J. An *et al.*, Science **324**, 1312 (2009).
[20] C.-C. Lu, Y.-C. Lin, Z. Liu *et al.*, ACS Nano **7**, 2587 (2013).
[21] T. Iwasaki, A. A. Zakharov, T. Eelbo *et al.*, Surf. Sci. **625**, 44 (2014).
[22] L. Sun, Z. Wang, Y. Wang *et al.*, Nat. Commun. **12**, 2391 (2021).
[23] V. Carozo, C. M. Almeida, B. Fragneaud *et al.*, Phys. Rev. B **88**, 085401 (2013).
[24] G. Trambly de Laissardière, D. Mayou, and L. Magaud, Nano Lett. **10**, 804 (2010).
[25] A. Luican, G. Li, A. Reina, J. Kong, R. R. Nair, K. S. Novoselov, A. K. Geim, and E. Y. Andrei, Phys. Rev. Lett. **106**, 126802 (2011).
[26] G. Tarnopolsky, A. J. Kruchkov, and A. Vishwanath, Phys. Rev. Lett. **122**, 106405 (2019).
[27] D. M. Kennes, J. Lischner, and C. Karrasch, Phys. Rev. B **98**, 241407(R) (2018).
[28] Y. Cao, V. Fatemi, A. Demir *et al.*, Nature (London) **556**, 80 (2018).
[29] Y. Cao, V. Fatemi, S. Fang *et al.*, Nature (London) **556**, 43 (2018).
[30] M. Serlin, C. L. Tschirhart, H. Polshyn *et al.*, Science **367**, 900 (2020).
[31] S. Shallcross, S. Sharma, E. Kandelaki, and O. A. Pankratov, Phys. Rev. B **81**, 165105 (2010).
[32] T. Ohta, A. Bostwick, T. Seyller, K. Horn, and E. Rotenberg, Science **313**, 951 (2006).
[33] Y. Zhang, T.-T. Tang, C. Girit *et al.*, Nature (London) **459**, 820 (2009).
[34] A. B. Kuzmenko, I. Crassee, D. van der Marel, P. Blake, and K. S. Novoselov, Phys. Rev. B **80**, 165406 (2009).
[35] E. V. Castro, K. S. Novoselov, S. V. Morozov, N. M. R. Peres, J. M. B. Lopes dos Santos, J. Nilsson, F. Guinea, A. K. Geim, and A. H. Castro Neto, Phys. Rev. Lett. **99**, 216802 (2007).
[36] K. F. Mak, C. H. Lui, J. Shan, and T. F. Heinz, Phys. Rev. Lett. **102**, 256405 (2009).
[37] P. Moon, Y.-W. Son, and M. Koshino, Phys. Rev. B **90**, 155427 (2014).
[38] L. Xian, S. Barraza-Lopez, and M. Y. Chou, Phys. Rev. B **84**, 075425 (2011).
[39] P. San-Jose and E. Prada, Phys. Rev. B **88**, 121408(R) (2013).
[40] G. Yu, M. I. Katsnelson, and S. Yuan, Phys. Rev. B **102**, 045113 (2020).
[41] S. Talkington and E. J. Mele, Phys. Rev. B **107**, L041408 (2023).
[42] G. Chen, L. Jiang, S. Wu *et al.*, Nat. Phys. **15**, 237 (2019).
[43] Y. Park, B. L. Chittari, and J. Jung, Phys. Rev. B **102**, 035411 (2020).
[44] J. Shin, B. L. Chittari, and J. Jung, Phys. Rev. B **104**, 045413 (2021).
[45] B. L. Chittari, G. Chen, Y. Zhang, F. Wang, and J. Jung, Phys. Rev. Lett. **122**, 016401 (2019).
[46] K. S. Novoselov, A. K. Geim, S. V. Morosov *et al.*, Nature (London) **438**, 197 (2005).
[47] E. McCann and V. I. Fal'ko, Phys. Rev. Lett. **96**, 086805 (2006).
[48] M.-Y. Choi, Y.-H. Hyun, and Y. Kim, Phys. Rev. B **84**, 195437 (2011).
[49] J. Hass, F. Varchon, J. E. Millán-Otoya *et al.*, Phys. Rev. Lett. **100**, 125504 (2008).
[50] R. de Gail, M. O. Goerbig, F. Guinea, G. Montambaux, and A. H. Castro Neto, Phys. Rev. B **84**, 045436 (2011).

[51] P. Moon and M. Koshino, Phys. Rev. B **85**, 195458 (2012).
[52] D. S. Lee, C. Riedl, T. Beringer, A. H. Castro Neto, K. von Klitzing, U. Starke, and J. H. Smet, Phys. Rev. Lett. **107**, 216602 (2011).
[53] K. Hejazi, C. Liu, and L. Balents, Phys. Rev. B **100**, 035115 (2019).
[54] Y.-H. Zhang, H. C. Po, and T. Senthil, Phys. Rev. B **100**, 125104 (2019).
[55] M. Anđelković, L. Covaci, and F. M. Peeters, Phys. Rev. Mater. **2**, 034004 (2018).
[56] T.-F. Chung, Y. Xu, and Y. P. Chen, Phys. Rev. B **98**, 035425 (2018).
[57] O. F. Namarvar, A. Missaoui, L. Magaud, D. Mayou, and G. Trambly de Laissardière, Phys. Rev. B **101**, 245407 (2020).
[58] C. De Beule, F. Dominguez, and P. Recher, Phys. Rev. Lett. **125**, 096402 (2020).
[59] C. De Beule, F. Dominguez, and P. Recher, Phys. Rev. B **104**, 195410 (2021).
[60] B. Tsim, N. N. T. Nam, and M. Koshino, Phys. Rev. B **101**, 125409 (2020).
[61] R. Kubo, J. Phys. Soc. Jpn. **12**, 570 (1957).
[62] R. Kubo, M. Yokota, and S. Nakajima, J. Phys. Soc. Jpn. **12**, 1203 (1957).
[63] S. M. João, M. Anđelković, L. Covaci, T. G. Rappoport, J. M. Viana Parente Lopes, and A. Ferreira, R. Soc. Open Sci. **7**, 191809 (2020).
[64] J. P. Santos Pires, S. M. João, A. Ferreira, B. Amorim, and J. M. Viana Parente Lopes, Phys. Rev. B **106**, 184201 (2022).
[65] J. P. Santos Pires, S. M. João, A. Ferreira, B. Amorim, and J. M. Viana Parente Lopes, Phys. Rev. Lett. **129**, 196601 (2022).
[66] X. Lin, H. Zhu, and J. Ni, Phys. Rev. B **101**, 155405 (2020).
[67] S. Shallcross, S. Sharma, and O. A. Pankratov, Phys. Rev. Lett. **101**, 056803 (2008).
[68] X. Lin and D. Tománek, Phys. Rev. B **98**, 081410(R) (2018).
[69] J. H. García, L. Covaci, and T. G. Rappoport, Phys. Rev. Lett. **114**, 116602 (2015).
[70] A. Weiße, G. Wellein, A. Alvermann, and H. Fehske, Rev. Mod. Phys. **78**, 275 (2006).
[71] S. M. João and J. M. Viana Parente Lopes, J. Phys.: Condens. Matter **32**, 125901 (2020).
[72] A. Bastin, C. Lewiner, O. Betbeder-Matibet, and P. Nozieres, J. Phys. Chem. Solids **32**, 1811 (1971).
[73] F. Ortmann, N. Leconte, and S. Roche, Phys. Rev. B **91**, 165117 (2015).
[74] I. Brihuega, P. Mallet, H. González-Herrero, G. Trambly de Laissardiŕe, M. M. Ugeda, L. Magaud, J. M. Gómez-Rodríguez, F. Ynduráin, and J.-Y. Veuillen, Phys. Rev. Lett. **109**, 196802 (2012).
[75] E. Suárez Morell, P. Vargas, L. Chico, and L. Brey, Phys. Rev. B **84**, 195421 (2011).
[76] R. Peierls, Z. Phys. **80**, 763 (1933).
[77] Z. F. Ezawa, *Quantum Hall Effects: Field Theoretical Approach And Related Topics*, 2nd ed. (World Scientific, Singapore, 2008).
[78] P. Sinha, S. Murakami, and S. Basu, Phys. Rev. B **102**, 085416 (2020).
[79] T.-N. Do, P.-H. Shih, H. Lin, D. Huang, G. Gumbs, and T.-R. Chang, Phys. Rev. B **105**, 235418 (2022).